Endoscopic tactile capsule for non-polypoid colorectal tumour detection

Domenico Camboni[1,2], Luca Massari[1,2], Marcello Chiurazzi[1,2], Renato Caliò[1,2], Joan Ortega Alcaide[1,2], Jessica D'Abbraccio[1,2], Evangelos Mazomenos[3], Danail Stoyanov[3], *Member, IEEE*, Arianna Menciassi[1,2], *Senior Member, IEEE,* Maria Chiara Carrozza[1,2], *Senior Member, IEEE*, Paolo Dario[1,2], *Fellow, IEEE*, Calogero Maria Oddo[1,2]*, *Member, IEEE*, Gastone Ciuti[1,2]*, *Member, IEEE*

Abstract— Objective: **In this work, an endoscopic tactile robotic capsule embedding miniaturized MEMS force sensors is presented. The capsule is conceived to provide automatic palpation of non-polypoid colorectal tumours during colonoscopic procedures, since they are characterized by a high degree of dysplasia, higher invasiveness and lower detection rates with respect to polyps.** *Methods:* **A first test was performed employing a silicone phantom that embedded a set of inclusions with variable hardness and curvature. In this scenario, a hardness-based classification was implemented, demonstrating detection robustness to curvature variation. By following a comparison of several well-known supervised classification algorithms, we chose a weighted 3-nearest neighbor classifier to detect the inclusions. We also introduced a bias force normalization model in order to make different acquisition sets consistent. The parameters of this model were chosen through a particle swarm optimization method. Additionally, an ex-vivo test was performed to assess the capsule detection performance when magnetically driven along a colonic tissue. An external permanent magnet positioned at the end-effector of an anthropomorphic robotic arm was used to drive the capsule. In this framework, lumps were identified as voltage peaks with a prominence depending on the total magnetic force applied to the capsule.** *Results:* **In a 94 % accuracy in hardness classification is achieved, while a 100% accuracy is obtained for the lump detection within a tolerance of 5 mm from the central path described by the capsule.** *Conclusion:* **In the real application scenario, we foresee our device aiding the physician to detect tumorous tissues.**

Index Terms— **Abnormal tissue localization; Robotic tissue palpation of non-polypoid tumours; Robotic endoscopic capsule; MEMS tactile sensors; Particle swarm optimization;** *ex-vivo* **phantom.**

I. INTRODUCTION

MEDICAL literature highlights the importance of detecting non-polypoid tumours (NPT) in colorectal endoscopy, in particular laterally spreading lesions larger than 10 mm. NPTs may be flat, slightly elevated or depressed, exhibiting submucosal invasion, even in the case of small neoplasms [2]. Colorectal lesions show a higher elastic modulus compared to non-cancerous tissues [1], as well as characteristic vascular patterns and sub-mucosal pit-patterns, generally observed through magnified endoscopy, narrow band imaging (NBI) or chromo-endoscopy techniques [3]–[5]. However, chromo-endoscopy has a slow learning curve requiring over 200 procedures for an endoscopist to be considered competent in the technic [5]. Clinical studies have reported high sensitivity and specificity for these techniques. A study conducted on 200 colorectal polyps reported a sensitivity and specificity of 90.5 % and 89.2 % for NBI with magnification, and of 91.7 % and 90 % respectively, for magnified end chromo-endoscopy [6]. On the other hand, NPTs are difficult to detect by inexperienced physicians [2]. Besides optical imaging techniques, ultrasound pills, using piezoelectric micro electro mechanic systems (MEMS), have also been researched to detect gastrointestinal tumours, as well as other diseases/conditions of the oesophagus[7], [8]. Similar technology is now featured in commercial endoscopes.

A. State of the Art and related work

The characteristic elastic modulus and submucosal pit pattern of colorectal tumours have inspired the design of tactile sensing devices for tumour detection in endoscopic procedures [9]–[12]. Moreover, tactile sensing devices were successfully used in several biomedical applications such as: RMIS, prosthesis and tissue characterization, [13]–[19].

C. M. Oddo are with The BioRobotics Institute of Scuola Superiore Sant'Anna, 56127 Pisa, Italy and with the Department of Excellence in Robotics & AI, Scuola Superiore Sant'Anna, 56127 Pisa, Italy (correspondence e-mails: gastone.ciuti@santannapisa.it and calogero.oddo@santannapisa.it).

E. Mazomenos and D. Stoyanov are with the Wellcome Trust / EPSRC Centre for Surgical and Interventional Sciences (WIESS), Centre for Medical Image Computing and the Department of Computer Science, University College London, London, WC1E 6BT, U.K.

TABLE I
TUMOUR PHANTOMS IN LITERATURE

Ref.	Phantom Shape	Surround material	Lump material	Lump shape
[29]	Rectangular 305 x 280 x 38 mm	EcoFlex 00-10	ABS	Spherical 3.5; 6.5; 9.5; 12.5; 15.5 mm in diameter
[30]	Tube 74mm internal diameter	Acrylic	Silicon (shore 30A to 60 A)	Disc-shape approx. Diam. around 36mm
[19]	Rectangular	Silicone RTV6166	Staedtler Mars plastic 526-50 (Shore 47 - 50A)	Spherical
[27]	Rectangular	Silicone (Shore 10A and 30A)	Urethane rubber (shore 30A, 40A and 60A)	Hemispherical (3.72; 6.35; 12.7; 25.4)
[21]	Rectangular 150x85x50 mm	Silicone (DSE 7310) [Y.mod. 12kPa]	PDMS [Y.mod. 200kPa]	Rectangular 50x10x15mm
[33]	Rectangular (no dimension) Rectangular (no dimension)	Gelatin (10.2gr/250ml) PVC plastisol (1.75:1)	Gelatin (28.8gr/250ml) PVC plastisol (pure liquid plastic)	Cubic (25mm side) Cubic (25mm side)
[20]	Cubic 32mm side approx.	Ecoflex 00-10 and Ecoflex 00-30	Delrin	Spherical (6.5, 9.5, 12.5mm diam.) depths of 1.5, 2.5, 3.5mm
[23]	Cubic	Ecoflex 00-30	Delrin	See table 1 [23]
[22]	Rectangular	Silicone Rubber 10 Shore 00	Solid plastic	Cylindrical
[59]	N.D.	Porcine Stomach	See Table 4 in [59]	Cubic (15x15x10 mm)
[32]	N.D.	Porcine Liver	Objet VeroWhite (Y. Mod. 1100 MPa)	Squared (16x16x2 mm)
[31]	N.D.	Porcine Liver (in-vivo)	Agar gelatine (30:1 mixture)	N.D.

1) Hardness detection

Many researchers have focused on the development of new sensing components used to detect hardness variations in soft tissues. Such works deals with the development of *ad-hoc* artificial phantoms while others deployed hard inclusions in *ex-vivo* or *in-vivo* animal tissue in order to assess the performance of their sensing components and detection strategies. TABLE I reports a brief overview of tumour phantoms, used for hardness or stiffness detection and reported in literature, with a focus on NPT tumours (hard mass included in a soft tissue with small or no prominence). Gwilliam *et al.* published a study comparing human and robotic sensing capabilities (employing a capacitive sensor), while localizing lumps in soft tissues; results show that the tactile sensor outperforms the human finger [20]. Ahn *et al.* proposed a palpation method for prostate cancer detection inspired by actual finger sweeping motion [21]. Ahmadi *et al.* built a beam-type optical sensor to measure the distribution of force in order to detect hardness in tissues [22]. Jia *et al.* demonstrated the capabilities of an elastomeric-based device, named GelSight, to detect lumps down to 2 mm in diameter. However, the GelSight requires the application of a force of 25 N on the tissue [23] (unbearable for a human bowel, which would perforate applying a force of about 13.5 N on a surface of 3.5 mm^2 [24]). Chuang *et al.* presented a 1.4 mm diameter piezoelectric tactile sensor for hardness detection which can fit into an endoscope. Its main drawback is the impossibility to detect hardness under static conditions. Also, even if the resulting force applied to the tissue was 0.6 N, they drove the sensor with 12 N at 1 Hz by employing a shaker [25], [26]. Arian *et al.* used a sensor resembling an artificial finger, called BioTac® to detect artificial tumours in the form of rubber inclusions into a silicone matrix, and provided haptic feedback to the user. The authors reported an average accuracy of 72 %, but it required the application of a 25 N force applied on the phantom [27]. Xie *et al.* build a tactile probe head, with a diameter of 14 mm, equipped with 14 tactile elements, each one ranging from 0 to 0.5 N with a resolution of 0.05 N. The authors reported an estimated output force exceeding 0.4 N during the palpation over hard inclusions, while a force of 0.15 - 0.25 N were recorded in nodule-free area [19]. Nichols *et al.* presented a method to segment hard inclusions from soft tissue by applying machine learning methods to data acquired with a load cell (Nano-17, ATI Industrial Automation, Apex, North Carolina, USA) attached to the end point of a robotic arm (Phantom Premium 1.5, Geomagic, Morrisville, North Carolina, USA). The authors reported a sensitivity above 0.95 and a specificity above 0.92 for this method, with a maximum stiffness ratio of 2.4 between hard and soft tissue [28]. Hui *et al.* published a study investigating the robustness of perceptual methods applied to tactile tumour detection. The authors claim an accuracy of 80% using a binary pairwise comparison method [29]. Furthermore, Winstone *et al.*, through a bioinspired remote tactile sensing endoscopic capsule, demonstrated using classifier systems (Support Vector Machine - SVM and Classifier Neural Network - CNN) the capability of detecting lumps of different shapes, sizes and hardnesses [30].

It is worth mentioning the work of Beccani *et al.*, who presented a wireless device for tissue palpation in laparoscopy [31], [32]. The tool is deployed and maneuverer by means of a trocar. The sensing element consists of a magnetic field sensor, which localizes the tool based on an external magnetic source. This allows estimating the reaction pressure and the indentation depth on the tissue. The device has demonstrated to detect lumps both in synthetic and *in-vivo* conditions with 5% and 8%

errors, respectively.

2) Automatic classification

Machine learning techniques have been employed to classify hard inclusions in soft tissues. Nichols *et al.* presented a method to segment hard inclusions using a Gaussian discriminant classifier. Its accuracy in segmenting 25 mm length inclusions was above 95 % [33]. Hui *et al.* employed the BioTac® finger and acquired two datasets from a silicone sample with hard lumps embedded. They showed that a Gaussian model trained on one dataset performs poorly on the other one. They proposed a binary pairwise comparison technique to match the two datasets which lead to a 80 % accuracy rate [29]. Winstone *et al.* introduced a bio-inspired tactile device, called TacTip, which measures its deformation due to the interaction with an object. The device consists of a deformable layer equipped with internal pins, which movement is optically detected. The authors demonstrated the device capabilities in classifying lumps of different size, shape and hardness [34]–[36]. They also trained a SVM classifier and a CNN to detect 3 mm silicone protuberant inclusions obtaining 81 % and 77 % accuracy rates, respectively [30].

B. Contribution

In this work, we demonstrate an endoscopic tactile capsule for automatic detection and classification of NPTs during colonoscopy. An early version of the capsule has been already presented demonstrating its capabilities to navigate applying a constant force on the tissue [37]. The capsule sensing mechanism is based on a MEMS tri-axial force sensor, originally developed for tactile restoration in upper limb prostheses [38], [39]. The same sensor has been used for MIS applications. A preliminary study of tactile tool for foetal surgery proved the reliability of the sensor [40]. Here, we employ the same sensing technology together with machine learning techniques to classify the hardness of rubber inclusions, independently of their curvature, in a silicone phantom (Fig. 2). Such inclusions are inserted in a phantom, avoiding protuberant lumps, and have size of 10 mm in order to resemble NPTs [2]. The robotic capsule palpates the phantom by sliding on it, and not just vertically indenting, in order to be consistent with a realistic magnetically-driven endoscopic procedure [41], [42]. The normal force applied on the tissue, while sliding, is 0.4 N, which is in line with what reported in literature for magnetically-driven capsule endoscopy [43], [44]. Then, we trained a weighted 3-nearest neighbor algorithm for classification and normalized the sensor outputs with the bias force applied to the tissue using a custom normalization model. The parameters of the normalization model were chosen based on a particle swarm optimization (PSO) in order to allow the device to be used with variable contact forces. We used different datasets for training and testing, thus addressing the issue of algorithm robustness discussed by Hui *et al.* in [29], and the results significantly outperform the literature.

The paper is organized as follows. The robotic tactile capsule is described in Section II.A. The two test protocols together with their relative data processing are reported respectively in Section II.B and Section II.C. Section III presents the results and Sections IV and V report the discussion and conclusions, respectively.

II. MATERIALS AND METHODS

A. Tactile capsule

The tactile capsule consists of an array of 4 tri-axial force MEMS sensors, with their conditioning electronics, and a 3D-printed body hosting a N50 NdFeB axially magnetized permanent magnet with dimensions 12 mm (l), 8 mm (w), and 8 mm (h). The magnetization axis is orthogonal to the sliding direction. The capsule is covered with Dragon Skin® 20 silicone (Smooth-on, Pennsylvania, USA), with a spherical dome over the sensors array as can be observed in Fig. 1(a). The capsule prototype dimensions are 33 mm (l), 26 mm (w), and 17 mm (h). Each MEMS force sensor is composed of a central pillar, which mechanically deflects 4 piezoresistive channels when in contact with an external body [38], [45] Fig. 1 (b) and Fig. 1 (c). The sensitivity of the bare MEMS force sensor ranges from around 30 mV/N to 60 mV/N between different sensors with a force range up to 3 N [46]–[48]. The voltage signal is acquired and conditioned from an ADC (Analog Digital Converter) with 16 channels and 24 bits resolution (ADS1258, Texas Instruments) [46]. The silicone elastic cover insulates the MEMS sensors and transduces the external forces applied on the sensors array, thus, influencing the performance of the MEMS sensors by extending the maximum range of perceived forces, while decreasing the sensitivity of the transducers [49]–[51].
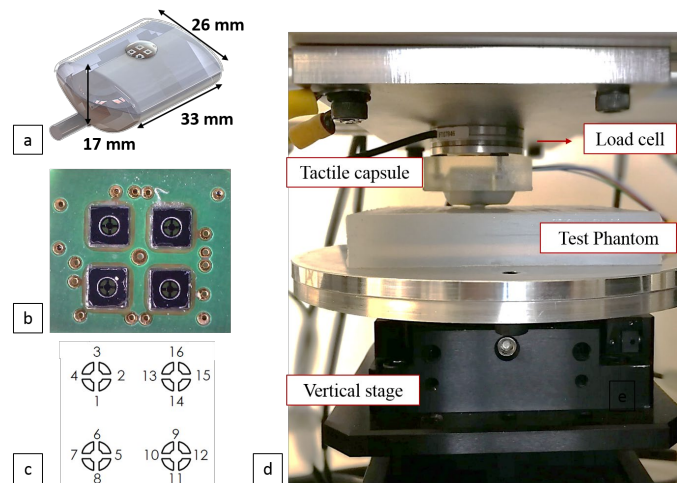

Fig. 1 - a) Rendering of the tactile capsule; b) microscope picture of the array of MEMS sensors embedded into the capsule; c) layout of the 4 MEMS sensors and 16 channels; d) experimental set-up composed of three micrometric stages programmatically controlled with a LabVIEW routine, a 6-axis load cell, the tactile capsule and a synthetic test phantom.

B. Test phantom and experimental set-up

The test phantom is composed of Dragon Skin® shore 10A (Smooth-on, Pennsylvania, USA) with dimensions 100 mm (l), 100 mm (w), and 17 mm (h). It embeds 5 lines of rubber inclusions (which are inserted to have no superficial lumps) with increasing hardness according to Fig. 2: *i)* DragonSkin®
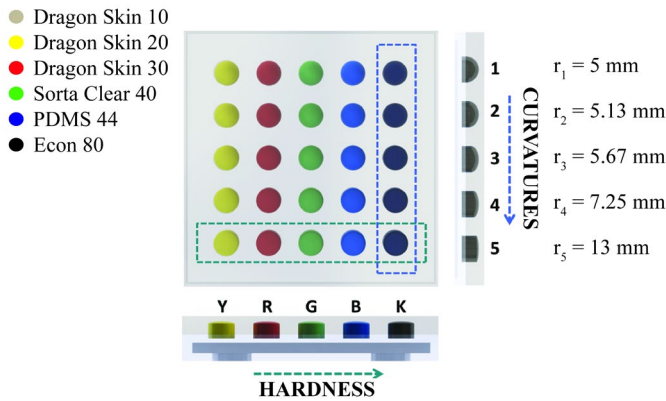
Fig. 2- Graphical representation of the silicone test phantom embedding rubber inclusions with different hardness and curvature. The Dataset 1 was collected by scanning the rows of the phantom, Dataset 2 scanning the columns.

shore 20A (yellow line, marked with the Y letter - Smooth-on, Pennsylvania, USA), *ii)* DragonSkin® shore 30A (red line, R - Smooth-on, Pennsylvania, USA), *iii)* SORTA-Clear® shore 40A (green line, G - Smooth-on, Pennsylvania, USA), *iv)* PDMS shore 44A, [52] (blue line, B - Sylgard 184, Dow Corning, USA), and *v)* Econ® shore 80A (black line, K - Smooth-on, Pennsylvania, USA). Within the present study, authors designed the phantom in order to reproduce the stiffness variation between tumours and healthy tissues (tumours are approximately 10 times stiffer than healthy tissues, [1]), instead of emulating the tissue mechanical properties that are difficult to be obtained in an in-vivo scenario. Each rubber inclusion has circular shaped base with 10 mm diameter, height of 5 mm, centre to centre distance of 17 mm from the neighboring lumps, and it is placed at 7 mm depth. Referring to Fig. 2, each column corresponds to a different radius of curvature, increasing according to the numeration, going from a semi-sphere (1) to a
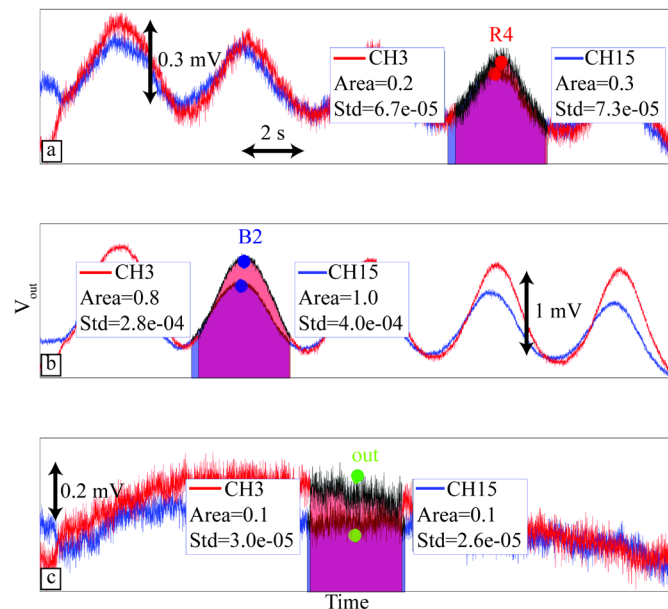

Fig. 3 - Feature representation on example voltage output data from channels 3 and 15, selected as the channels with the most significant output signal with respect to the experimental conditions. Three different scanned lines, with highlighted inclusions: a) dragon skin 30, curvature 4 (R4), b) PDMS, curvature 2 (B2) and c) no inclusion (out).

cylinder (5). The term curvature refers to the radius of the embedded lumps in the used phantom (both synthetic and *ex-vivo*).

The capsule is mounted on a 3D-printed support, and it is fixed while the test phantom moves below it. A 6-axis load cell (Nano 43, ATI Industrial Automation, Apex, NC, USA) is placed just over and connected to the capsule, in order to measure the force acting on the capsule while sliding. In parallel with the MEMS sensors responsible for measuring local interaction Fig. 1 (d). The test phantom is moved by a set of three motorized micrometric stages: an 8MTF-102LS05 *x-y* stage and an 8MVT120-25- 4247 vertical positioner, (Standa, Vilnius, Lithuania). Motors are programmatically controlled by a LabVIEW routine.

1) Experimental test protocol

The test phantom is moved vertically, along the *z* axis, to approach the capsule Fig. 1 (d). The indentation stops when a threshold force of 0.4 N is reached, based on the load cell measures. Then, after a pause of 2 s, it starts sliding, moving in position control along the x-axis for 85 mm, with a speed of 5 mm/s, which represents the average operating speed for a magnetically-driven capsule endoscopy [43], [44]. The phantom is horizontally scanned: one scan for each line of rubber inclusions, plus one on a line without any inclusions (hereafter called *out*). The aforementioned experimental protocol is repeated 5 times.

Two datasets are acquired by placing the test phantom in two different configurations. According to Fig. 2, the *Dataset 1* (DS 1) is obtained by scanning the rows of the test phantom, *i.e.* for each scan the capsule runs on inclusions of different material (different hardness) but with the same curvature. By rotating the phantom of 90 degrees, the *Dataset 2* (DS 2) is acquired by sliding on the columns of Fig. 2, thus experiencing inclusions of same material but with different curvature. Each dataset contains 30 scans per iteration of the protocol (from the 25 different rubber inclusions of the test phantom, plus 5 related to the line *out*). This sums up to 150 measurements considering that the protocol is repeated 5 times.

2) Data pre-processing and features extraction

The acquired data are processed off-line with Matlab® (MathWorks, Inc., MA, USA). For each scan, the array corresponding to the voltage output of each MEMS channels is programmatically divided in 5 parts (hereafter named inclusions) to isolate the peaks contained (see Fig. 3(a)). Even the line with no rubber inclusions (*out*) is divided in 5 parts. All the arrays have same length and the peaks of the inclusions are located in the middle of the arrays. The minimum value of the whole scan is subtracted to each of them, and they are labelled according with the naming given to the rubber inclusions in Fig. 2, *i.e.* a letter for the material and a number for the curvature (*e.g.* Y4 stands for DragonSkin® shore 20, curvature 4).

Two features are associated to MEMS data gathered while interacting with each inclusion: *i)* the area, and *ii)* the standard deviation. These values are related to the hardness and the curvature of the material, respectively. Such features are used

as predictors for the classification algorithm. Fig. 3 shows examples of raw voltage outputs from channels 3 and 15 (single inclusions are highlighted; the label associated to them and the related features are reported).

3) Normalization with the bias force

As expected, either little imperfections in positioning the phantom, or small variations in the indentation force can lead to significant changes in the inclusion features. Fig. 4 (a) shows how the features vary in the two datasets (curvature and hardness) and across the different materials (change in hardness). Ideally, the two datasets should overlay, being representations of the same items. On the other hand, in order to be correctly classified, each material should be isolated from the other ones. However, since the capsule is moved without continuous force-feedback control, the contact force fluctuation can be significant, leading to misalignments across the different hardness (*e.g.* R-Y and K have huge overlaps). For this reason, it is important to normalize the features with the bias force affecting the capsule and monitored by the load cell. The following model of normalization with respect to the force has been adopted for correction:

$$\vec{F_l} = a_i \vec{F_x} + b_i \vec{F_z}$$

$$Area_i|_{norm} = Area_i/(c_i F_i)^m \qquad (1)$$

$$Std_i|_{norm} = Std_i/(d_i F_i)^n$$

where the i subscript stands for the channel number. So, for each i channel, the normalization force F_i is given by a different combination of F_x and F_z. But also, the two features (*i.e.* area and standard deviation) have a different relationship with the applied force, which is described by the coefficients c_i, d_i, and m, n, which are constant for all channels. After the normalization, as shown in Fig. 4 (b) , the datasets regrouped closer, but clearly separated for each hardness.

Particle Swarm Optimization is adopted to solve this multi-dimensional problem. One more variable for each channel is added to enable the algorithm to switch off a number of channels in order to improve the performances. After each iteration, the classifier is trained according to the subset of channels in use, and the classifier loss resulting from the test is used as cost function. Upper and lower bounds, x_U and x_L, have been set to 1 and 0.01 for all the variables, except m and n, which upper bound has been chosen to be 3 (zero has been excluded to avoid division by zero). The other PSO parameters are: *i)* number of iterations 1000, *ii)* population size 50, *iii)* inertia coefficient w 0.72, *iv)* cognitive acceleration and social acceleration coefficients, c_1 and c_2, equal to 1.49 [53].

4) Classification algorithm

Two types of classification tests have been conducted in order to choose the classification algorithm: *i) hardness classification*, involving 6 classes, which refer to the 5 different types of material plus the *out*, and *ii) hardness and curvature classification*, considering all the 26 classes resulting by aggregating material and curvature information, plus *out*. These

tests are performed on the single datasets (DS 1 and DS 2), and also merging the two (DS 1,2).

Several supervised classification algorithms have been considered as potential candidates. More specifically, we have compared: *i)* Support Vector Machine (SVM), with quadratic, cubic and Gaussian kernels; *ii)* Linear Discriminant; *iii)* k-nearest neighbor (kNN); and *iv)* weighted k-nearest neighbor. For kNNs, we have performed an exhaustive comparison by varying the number of neighbors from 1 to 10, also considering all the possible combinations of channels subset. The algorithms have been compared based on a 5-fold cross-validation, without involving force normalization. Then, the best classifier has been trained on DS 1, and tested on DS 2, by applying bias force normalization, only for *Hardness classification* (which has clinical relevance for tumour detection).

C. Ex-vivo tests and experimental set-up

The *ex-vivo* phantom is presented in Fig. 5 (b). The phantom consists of a Dragon Skin® shore 10A (Smooth-on, Pennsylvania, USA) with dimensions 300 mm (l), 70 mm (w), and 6.5 mm (h) and with 15 PDMS shore 44A inclusions embedded in it [52]. The phantom surface is flat since all the rubber inclusions are covered by Dragon Skin® shore 10A. The inclusions are randomly placed within a 34 mm width strip,
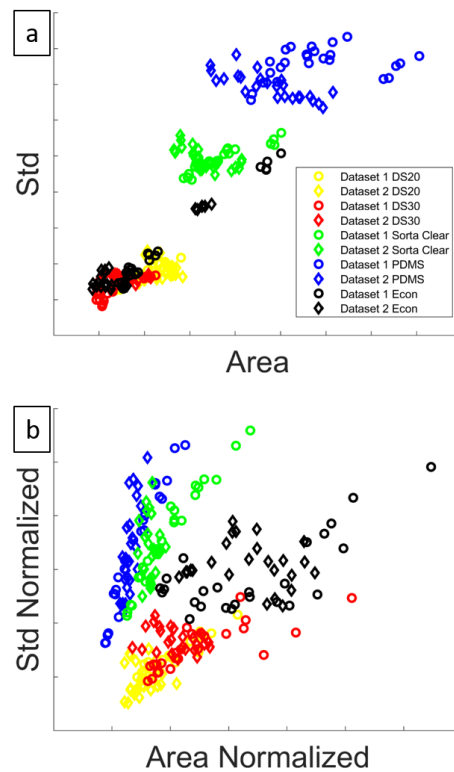

Fig. 4 Representation of features associated to the different datasets and across the different materials: a) area function of the standard deviation, and b) area function of the standard deviation normalized with the bias force.

centred on the median along the y-axis and with a pace of 19 mm along the x-axis as presented in Fig. 9 (g). Each PDMS inclusion is a 5 mm radius hemisphere (*i.e.* curvature r1 in Fig. 2). The outer surface of this polymer-based phantom is lined
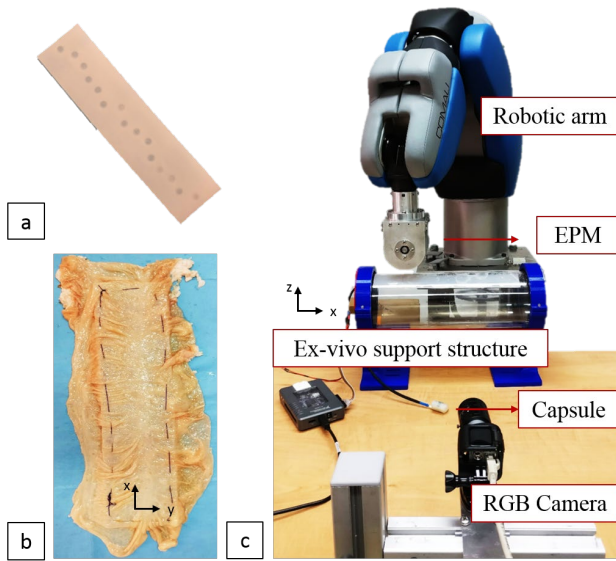
Fig. 5-*Ex-vivo* experimental set-up: a) silicone phantom, b) *ex-vivo* animal tissue sewed on the silicone phantom, and c) experimental set-up.

with a sample of fresh explanted swine large intestine. Such a coating has been sewed to the silicone to obtain a flat *ex-vivo* phantom mimicking the properties of NPTs.

1) Experimental test protocol

As shown in Fig. 5, the set-up used for the *ex-vivo* test consists of a N52 NdFeB external permanent magnet (EPM), with cylindrical shape (radius 45 mm and height 80 mm), integrated with the end-effector of an anthropomorphic robotic arm (Racer3, Comau S.p.A, Turin, Italy) Fig. 5 (a). By translating the EPM, a magnetic force along the x-axis is imposed to the capsule causing it to translate, mimicking real conditions. The tissue is stitched to the phantom Fig. 5 (b) and fixed to the structure as showed in Fig. 5 (c). Unlike in tests
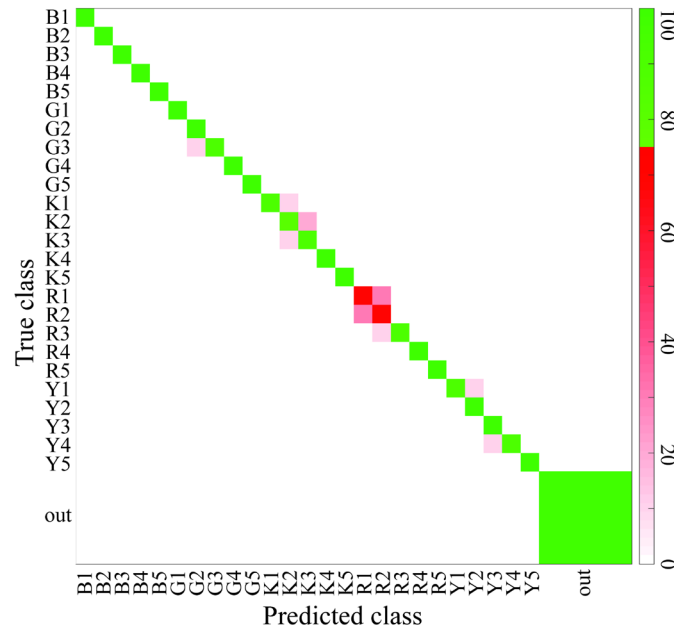

Fig. 6 - Accuracy (94.7 %) of training and validation of a weighted 3-NN classifier for hardness and curvature discrimination, trained with both the curvature and hardness Datasets (5-fold cross-validation).

TABLE II
CLASSIFIERS ACCURACY COMPARISON

Classifier	Hardness			Hardness and curvature		
	DS 1	DS 2	DS 1,2**	DS 1	DS 2	DS 1,2*
Quadratic SVM	100	100	100	98.7	94.7	93
Cubic SVM	100	100	100	98.7	92.7	91
Gaussian SVM	100	99.3	100	98	88	93.3
Linear Discrim.	99.3	100	95.7	98.7	91.3	76.7
1-kNN	100	100	100	96	83.3	92.7
3-wkNN	**100**	**100**	**100**	**96.7**	**94.7**	**94.7**
10-wkNN	100	99.3	100	94.7	86.7	89.3

* Result obtained without bias force normalization, by merging the two Datasets.

with the synthetic phantom, the capsule was equipped on the top side with a rigid plastic cover leaving exposed the capsule sensible area. In order to monitor the position of the capsule within a specific plane , a 2D RGB camera (Basler ACE, 1300-30gc, Ahrensburg, Germany) Fig. 5 (c) was integrated with the experimental set-up detecting and tracking an *ad-hoc* target, 3D printed and fixed to the capsule bottom.

We positioned the EPM on top of the capsule at two different relative distances (h) and then moved for 200 mm (Δx) linearly along the x-axis at 5 mm/s. Then the capsule was manually positioned at its initial position. Three independent trials for each of the two tested distances (short distance h_1 equal to 45 mm, large distance h_2 of 65 mm) were performed in order to evaluate system repeatability. It is worth mentioning that the selected distances were chosen in order to guarantee a magnetic navigation force compatible with the integrated magnets (not optimized for real magnetic colonoscopy). During each trial, the force sensed by the capsule (16 channels), the robot end-effector position (X, Y, Z), and the capsule position monitored through the 2D camera (X, Y) at a frequency of 380 Hz, were recorded. Moreover, for each test, the robot end-effector velocity and its relative distance with the *ex-vivo* phantom were maintained constant due to a precise positioning control of the robotic end-effector (estimated error in the Cartesian space within 0.1 mm).

2) Data processing and lump detection

In order to detect the embedded lumps, we assumed static conditions and small tissue displacements so that the tissue in contact with the capsule could be modelled as a linear elastic material. The applied magnetic force on the capsule surface is supported as follows (Eq. 2).

$$F_{magnetic} = \int_{A_{total}} k(x,y)\Delta L dA$$
$$= \int_{A_{sensorized}} (1_{A_{soft}} k_{soft} + 1_{A_{stiff}} k_{stiff}) \Delta L dA \qquad (2)$$
$$+ \int_{A_{blind}} (1_{A_{soft}} k_{soft} + 1_{A_{stiff}} k_{stiff}) \Delta L dA$$

where k_{soft} represents the stiffness of the soft surrounding material, k_{stiff} ($> k_{soft}$) represents the stiffness of the lumps, ΔL represents the depth of the phantom compression, A represents the area, and $1_{A_{stiff}}$ is a discrete function that takes the value of

TABLE III
PSO OPTIMUM SOLUTION

Parameter	Channel 11	Channel 12	Channel 15
A	0.01	0.17	0.01
b	1	1	1
c	0.43	1	0.74
d	0.93	0.87	0.7
m		2.41	
n		1.51	

The channels that have been disabled by the optimization process are not reported in the table.

1 in the stiff region and 0 elsewhere (*vice versa* for $1_{A_{soft}}$). It is clear from (**2**) that, for a known magnetic force applied, the force sensed by the capsule will be higher when the sensible area is placed on top of a locally stiffer surface. It is also relevant to mention that the model predicts that, for a given hardness distribution of the tissue, the sensed force will vary proportionally to the magnetic force applied, which will be known when using the capsule [54].

The acquired data are processed off-line with Matlab® (MathWorks, Inc., Natick, Massachusetts, USA). For each scan, the array corresponding to the voltage output of each MEMS channels is isolated in order to compute the peaks contained. Each test starts with the EPM centre of gravity positioned vertically on top of the sensitive capsule at one of the two tested distances (h_1 or h_2). The measured voltages of each of the capsule sensor channels at this starting condition are used as sensor offsets for the rest of the experiment. Thus, sensor variation from its baseline is monitored and used in order detect lumps once a specific threshold is exceeded. In particular, a lump has been defined to be a local peak with a prominence larger than 0.4 mV for the short distance tests and of 0.25 mV for the large distance tests. A lump has been identified using the sum signal of the selected 4 capsule sensor channels. The change of peak prominence threshold is inversely related to the total force applied at the capsule. Starting from the achieved results, a confusion matrix is then built up in order to analyse the number of lumps correctly detected.

In a real scenario, where the gastrointestinal environment shows a complex 3D configuration, a magnetic closed loop navigation by means of a capsule localization system is fundamental to calculate the magnetic interaction force in order to continuously set the sensor baseline for an accurate local force monitoring based on the embedded MEMS [55].

III. RESULTS

A. Synthetic phantom test

1) Classifiers comparison

The results of the classifiers comparison are summarized in TABLE II. The Quadratic SVM and the weighted 3-NN achieved the best performances. Although the two have comparable results in terms of accuracy (*i.e.* correct predictions divided by the total number of predictions), the weighted 3-NN is much faster because of the lower computational cost (3700 observations per second versus 200, for the Quadratic SVM). Therefore, we chose the weighted 3-NN as our best performing method, which would be more suitable for a future real-time application of the classification method. The *hardness classification* obtained by merging both the datasets (DS 1,2) has a 100 % accuracy, after a 5-fold cross-validation. While addressing the additional classification of curvature information, and therefore enlarging the number of classes to 26, the *hardness and curvature classification* with the weighted 3-NN classifier has 94.7 % accuracy. Fig. 6 shows a confusion matrix of this classification test. It is worth noting that the errors refer only to neighboring curvatures, *e.g.* R2 is misclassified with R1 or R3, but neither with R5, nor with items of other materials.

2) Classification with bias force normalization

A weighted 3NN *hardness classifier* (on 6 classes) trained on DS 1 and tested on DS 2, and applying the bias force normalization, has 94 % accuracy, Fig. 8 (b). The model described in (1), with the parameters defined by the PSO involves only the channels 11, 12 and 15. The complete solution of the PSO is summarized in TABLE III. It is worth noting that a weighted 3NN classifier, without bias force normalization,
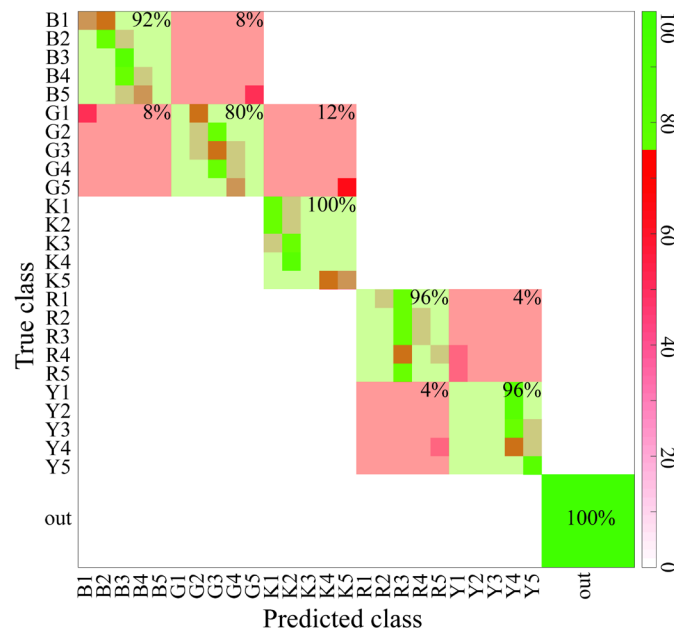

Fig. 7. Accuracy (31.5%) of training and validation of a weighted 3-NN classifier for hardness and curvature discrimination, trained with Dataset 1 and tested with Dataset 2, and applying the bias force normalization model.
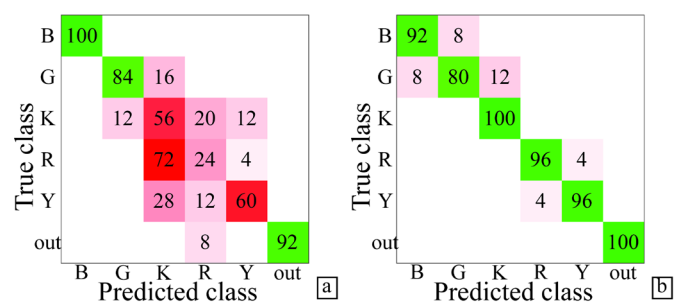

Fig. 8 - Accuracy of a weighted 3-NN classifier for hardness discrimination (channels in use: 11, 12 and 15), trained with Dataset 1 and tested with Dataset 2: a) without bias force normalization (69 % accuracy), and b) with bias force normalization (94 % accuracy).

TABLE IV
PERCENTAGE OF LUMPS DETECTED ALONG THE PHANTOM

Lumps	1	2	3	4	5	6	7	8	9
Short distance	100%	100%	100%	0%	100%	100%	33%	100%	67%
Long distance	100%	100%	100%	33%	100%	100%	0%	100%	0%

using all available channels has 47 % accuracy, and restricting to the channels selected by the PSO, but without normalization, has 69 % accuracy, Fig. 8 (a). This confirms that different sets of acquisition, having different bias forces, are not consistent if not normalized. It is worth mentioning that such classifications are consistent with the results highlighted in Fig. 4. Indeed, it is evident that before the normalization misclassification mainly occurs between the Y-R and K materials, that show huge overlaps in the graph. While, after normalization, since the points representing the different materials in the graph are separated, accuracy increases.

B. Ex-vivo tests

The lump detection results are presented in TABLE IV. The lump detection resulted in two false positives within 2 mm of the lump projection on the x-axis, Fig. 9 (g). On the other hand, 6 out of the 9 lumps were always detected for both manipulation distances and the fourth lump was never detected. Fig. 9 presents the results obtained for both the evaluated distances. Is important to note that the only indicator used to identify a lump has been the peak prominence. Such indicator can be evaluated online just depending on the total force applied to the capsule, which can be predicted if the relative pose between the EPM and the capsule is known [55].
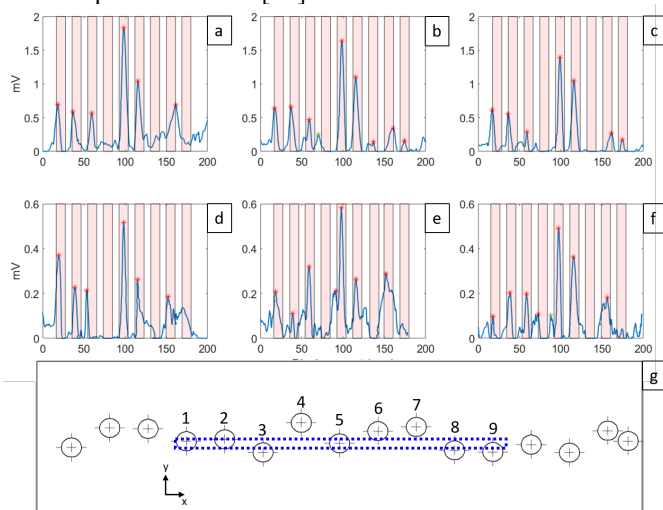

Fig. 9 - Panels (a-f) show the average signal of the four capsule channels used (6, 7, 10 and 12) to detect the lumps. Panels (a-c) present the tests performed with the EPM moving at 45 mm (short distance) on top of the capsule while (d-f) present the results when the EPM moved at 65 mm (large distance) on top of the capsule. The red strips represent the projection of the lumps into the capsule path. Red and green marks identify the lumps detected using the proposed method. Red marks are lumps detected within the expected lump location while green marks are lumps detected outside of the expected lump location. In panel (g), the path executed by the EPM on top of the phantom is highlighted.

IV. DISCUSSION

A. Synthetic phantom test

The results obtained with this system, combining both the proposed device and the chosen classification method, give almost perfect results in terms of *hardness classification*.

For the sake of completeness, even if out of the main topic of this work, we tried a *hardness and curvature classification* test, with bias force normalization. Anyhow, the optimization process has been affected by stagnation. The problem we tried to solve has 47 dimensions and the local minima are at least 511 (equal to all the possible channels combinations) times the number of classes to discriminate. So, going from the 6 classes of the *hardness classification* to the 26 of the *hardness and curvature classification*, the local minima almost increase fivefold. The PSO algorithm tends to converge quickly to the swarm minimum, leaving potentially out of the search the actual global minimum. Fig. 7 shows that the classifier which performed 94% for hardness detection drops to 31.5% accuracy enlarging to 26 classes, (involving the bias force normalization reported in TABLE III). We also run a PSO with the purpose to maximize *hardness and curvature* classification, but we did not exceed 49% accuracy. Nonetheless, the results shown in Fig. 7 do not present errors related to the *out* class, which is always discriminated from all the other items. Furthermore, we can see that the items are almost exclusively misclassified with their immediate neighbors.

B. Ex-vivo tests

The presented results demonstrate that the interpretation of the sensed forces, by means of a static elastic model of the tissue interaction, is sufficient to successfully detect lumps embedded in a silicone phantom covered with *ex-vivo* animal tissue (TABLE IV). Such results prove the capability of the capsule to perform tissue palpation in order to identify regions of interest to further analyse and label the tissue as malign or benign using the presented classification method.

To the best of our knowledge this is the first time that a magnetically driven capsule, presenting tactile force sensors on its surface, is exploited for NPT detection in endoscopy both on artificial phantom and *ex-vivo* animal tissues. Compared to related works, [10], [18], [19], [23], [32], [34], [56], [57], our capsule shares the scope of tactile palpation for diagnostics for different medical applications. A biomimetic tactile capsule for endoscopic procedures was proposed by Winstone *et al*., [34], [57], whereas, diverging from our study, the experiments were performed using a rigid link to drive the capsule. Moreover, the invasiveness of our system is definitely lower due to the reduced dimensions (close to a real capsule dimension) and

thanks to the magnetically driven navigation approach [58].

V. CONCLUSIONS

In this work, an endoscopic tactile capsule for NPT automatic detection based on hardness classification, that is also compatible with applications in laparoscopy, has been presented. The prototype consists of an array of piezoresistive MEMS force sensors. There is potentiality for further dimensional scalability of the system, to make it compatible with the standards of colonoscopy (up to 16-17 mm (Φ) and 26-32 mm (l)). The device has been used for a proof of concept in a synthetic environment and results show a good accuracy, up to 94%, in discriminating different inclusions in a soft tissue, based on hardness. The low computational cost (3700 observations per second) allows translating this method into a real-time algorithm, in order to perform future tests in operative conditions. As arisen from the experiments, the device needs a calibration test before operation, in order to define the parameters for the force normalization algorithm.

In the real application scenario we foresee for our device, the tactile capsule is magnetically pulled by an external robotic arm equipped with a permanent magnet mounted on its tip. The capsule will be navigated by the physician towards a suspected lesion, which will be recognized with the help of image-based tools, and then a classification based on hardness will contribute evaluating whether the tissue is tumorous or not. A model that generalizes the sensors reading with the bias force makes the hardness classification robust and allows training the classifier with a subset of indentation forces, since the bias force model can generalize the output to a generic indentation force. The model we obtained with a heuristic optimization shows good results for the purposes of this study, *i.e.* discriminating areas with different hardness while sliding onto a surface. Furthermore, in the realistic scenario, a capsule magnetic localization system plays a central role. The localization output and magnetic force calculation will provide the F_x and F_z components to the normalization model and therefore the tactile system reliability will be significantly conditioned by the magnetic localization accuracy. For such magnetic navigation and localization system, currently under development, we expect a position error around ±5 mm, leading to a worst-case force error of ±40 mN.

The obtained results pave the way for further engineering and clinical studies, including hardness classification in *ex-vivo* conditions that will be part of a future extensive and focused contribution in the field of advanced diagnostics for endoscopic procedures, together with complementary *in-vivo* tests.

VI. REFERENCES

[1]   S. Kawano *et al.*, "Assessment of elasticity of colorectal cancer tissue, clinical utility, pathological and phenotypical relevance," *Cancer Sci.*, vol. 106, no. 9, pp. 1232–1239, 2015.

[2]   A. Facciorusso, M. Antonino, M. Di Maso, M. Barone, and N. Muscatiello, "Non-polypoid colorectal neoplasms: Classification, therapy and follow-up: 2015 Advances in Colorectal Cancer," *World J.*

[3]   S. Kudo, S. Tamura, T. Nakajima, and H. Yamano, "Diagnosis of colorectal tumorous lesions by magnifying endoscopy," *Gastrointest. Endosc.*, vol. 44, no. 1, pp. 0–6, 1996.

[4]   G. Ciuti, R. Caliò, D. Camboni, L. Neri, F. Bianchi, and A. Arezzo, "Frontiers of robotic endoscopic capsules : a review," *J. Micro-Bio Robot.*, pp. 1–18, 2016.

[5]   J. E. East *et al.*, "Narrow band imaging with magnification for the characterization of small and diminutive colonic polyps : pit pattern and vascular pattern intensity," *Endoscopy*, vol. 10, pp. 811–817, 2008.

[6]   J. J. W. Tischendorf *et al.*, "Value of magnifying chromoendoscopy and narrow band imaging (NBI) in classifying colorectal polyps : a prospective controlled study," *Endoscopy*, vol. 39, no. 12, pp. 1092–1096, 2007.

[7]   Y. Qiu *et al.*, "Piezoelectric micromachined ultrasound transducer (PMUT) arrays for integrated sensing, actuation and imaging," *Sensors (Switzerland)*, vol. 15, no. 4, pp. 8020–8041, 2015.

[8]   S. Trolier-Mckinstry *et al.*, "Designing piezoelectric films for micro electromechanical systems," *IEEE Trans. Ultrason. Ferroelectr. Freq. Control*, vol. 58, no. 9, pp. 1782–1792, 2011.

[9]   M. Baumhauer, M. Feuerstein, H. P. Meinzer, and J. Rassweiler, "Navigation in Endoscopic Soft Tissue Surgery - Perspectives and Limitations," *J. Endourol.*, vol. 22, no. 4, pp. 1–15, 2008.

[10]   S. Schostek, M. J. Binser, F. Rieber, C. N. Ho, M. O. Schurr, and G. F. Buess, "Artificial tactile feedback can significantly improve tissue examination through remote palpation," *Surg. Endosc.*, vol. 24, no. 9, pp. 2299–2307, 2010.

[11]   M. I. Tiwana, S. J. Redmond, and N. H. Lovell, "A review of tactile sensing technologies with applications in biomedical engineering," *Sensors Actuators A Phys.*, vol. 179, pp. 17–31, 2012.

[12]   E. Sadovnichy, Victor and Gabidullina, Rozaliya and Sokolov, Mikhail and Galatenko, Vladimir and Budanov, Vladimir and Nakashidze, *Haptic device in endoscopy*. 2014.

[13]   A. Bicchi, P. Iacconit, and E. P. Scilingo, "A Sensorized Minimally Invasive Surgery Tool for Detecting Tissutal Elastic Properties," *IEEE Int. Conf. Robot. Autom.*, no. April, pp. 884–888, 1996.

[14]   P. Puangmali, K. Althoefer, L. D. Seneviratne, D. Murphy, and P. Dasgupta, "State-of-the-art in force and tactile sensing for minimally invasive surgery," *IEEE Sens. J.*, vol. 8, no. 4, pp. 371–381, 2008.

[15]   J. Konstantinova, A. Jiang, K. Althoefer, P. Dasgupta, and T. Nanayakkara, "Implementation of tactile sensing for palpation in robot-assisted minimally invasive surgery: A review," *IEEE Sens. J.*, vol. 14, no. 8, pp. 2490–2501, 2014.

[16]   C. Pacchierotti, S. Member, D. Prattichizzo, S. Member, and K. J. Kuchenbecker, "Cutaneous Feedback of Fingertip Deformation and Vibration for Palpation in Robotic Surgery," *IEEE Trans. Biomed.*

Eng., vol. 63, no. 2, pp. 278–287, 2016.

[17] P. Polygerinos, A. Ataollahi, T. Schaeffter, R. Razavi, L. D. Seneviratne, and K. Althoefer, "MRI-Compatible Intensity-Modulated Force Sensor for Cardiac Catheterization Procedures," *IEEE Trans. Biomed. Eng.*, vol. 58, no. 3, pp. 721–726, 2010.

[18] P. Puangmali, H. Liu, L. D. Seneviratne, P. Dasgupta, and K. Althoefer, "Miniature 3-axis distal force sensor for minimally invasive surgical palpation," *IEEE/ASME Trans. Mechatronics*, vol. 17, no. 4, pp. 646–656, 2012.

[19] H. Xie, H. Liu, L. D. Seneviratne, and K. Althoefer, "An optical tactile array probe head for tissue palpation during minimally invasive surgery," *IEEE Sens. J.*, vol. 14, no. 9, pp. 3283–3291, 2014.

[20] J. C. Gwilliam and E. Jantho, "Human vs . Robotic Tactile Sensing : Detecting Lumps in Soft Tissue," *2010 IEEE Haptics Symp.*, pp. 21–28.

[21] J. Kim, "Robotic palpation and mechanical property characterization for abnormal tissue localization," *Med. Biol. Eng. Comput.*, vol. 50, no. 9, pp. 961–971, 2012.

[22] R. Ahmadi, S. Arbatani, M. Packirisamy, and J. Dargahi, "Micro-optical force distribution sensing suitable for lump/artery detection," *Biomed. Microdevices*, vol. 17, no. 1, 2015.

[23] X. S. Jia and E. H. Adelson, "Lump Detection with a GelSight Sensor," *2013 World Haptics Conf.*, no. c, pp. 175–179, 2013.

[24] E. A. M. Heijnsdijk, M. Van Der Voort, H. De Visser, J. Dankelman, and D. J. Gouma, "Inter- and intraindividual variabilities of perforation forces of human and pig bowel tissue," *Surg. Endosc. Other Interv. Tech.*, vol. 17, no. 12, pp. 1923–1926, 2003.

[25] C. Chuang, T. Li, I. Chou, and Y. Teng, "Sensors and Actuators A : Physical Piezoelectric tactile sensor for submucosal tumor detection in," *Sensors Actuators A. Phys.*, vol. 244, pp. 299–309, 2016.

[26] Y. City, "PIEZOELECTRIC TACTILE SENSOR FOR SUBMUCOSAL TUMOR HARDNESS DETECTION IN ENDOSCOPY Department of Mechanical Engineering , Southern Taiwan University of Science and Technology , Kuang Tai Metal Industrial Co ., Ltd ., Kaohsiung , Taiwan Sensor fabrication," pp. 871–875, 2015.

[27] M. S. Arian, C. A. Blaine, G. E. Loeb, and J. A. Fishel, "Using the BioTac as a tumor localization tool," *IEEE Haptics Symp. HAPTICS*, no. Figure 1, pp. 443–448, 2014.

[28] K. A. Nichols and A. M. Okamura, "Methods to Segment Hard Inclusions in Soft Tissue During Autonomous Robotic Palpation," *IEEE Trans. Robot.*, vol. 31, no. 2, pp. 344–354, 2015.

[29] J. C. T. Hui, A. E. Block, C. J. Taylor, and K. J. Kuchenbecker, "Robust tactile perception of artificial tumors using pairwise comparisons of sensor array readings," *IEEE Haptics Symp. HAPTICS*, vol. 2016-April, pp. 305–312, 2016.

[30] B. Winstone, C. Melhuish, T. Pipe, M. Callaway, and S. Dogramadzi, "Toward Bio-Inspired Tactile Sensing Capsule Endoscopy for Detection of Submucosal

Tumors," *IEEE Sens. J.*, vol. 17, no. 3, pp. 848–857, 2017.

[31] M. Beccani *et al.*, "Wireless Tissue Palpation for Intraoperative Detection of Lumps in the Soft Tissue," *IEEE Trans. Biomed. Eng.*, vol. 61, no. 2, pp. 353–361, 2014.

[32] M. Beccani, C. Di Natali, M. E. Rentschler, and P. Valdastri, "Wireless tissue palpation: Proof of concept for a single degree of freedom," *Proc. - IEEE Int. Conf. Robot. Autom.*, pp. 711–717, 2013.

[33] K. A. Nichols, S. Member, and A. M. Okamura, "Methods to Segment Hard Inclusions in Soft Tissue During Autonomous Robotic Palpation," *IEEE Trans. Robot.*, vol. 31, no. 2, pp. 344–354, 2015.

[34] B. Winstone, G. Griffiths, and T. Pipe, "TACTIP - Tactile Fingertip Device , Texture Analysis through Optical Tracking of TACTIP - Tactile Fingertip Device , Texture Analysis Through Optical Tracking of Skin Features," *Conf. Biomim. Biohybrid Syst.*, no. May, pp. 323–334, 2013.

[35] B. Winstone, C. Melhuish, S. Dogramadzi, and T. P. M. Callaway, "A Novel Bio-inspired Tactile Tumour Detection Concept for Capsule Endoscopy," *Conf. Biomim. Biohybrid Syst.*, pp. 442–445, 2014.

[36] B. Winstone, T. Pipe, C. Melhuish, and S. Dogramadzi, "Biomimetic Tactile Sensing Capsule," *Conf. Biomim. Biohybrid Syst.*, no. July, pp. 113–125, 2015.

[37] R. Caliò *et al.*, "Robotic endoscopic capsule for closed-loop force- based control and safety strategies," *IEEE Int. Conf. Cyborg Bionic Syst.*, pp. 253–256, 2017.

[38] L. Beccai *et al.*, "Design and fabrication of a hybrid silicon three-axial force sensor for biomechanical applications," *Sensors Actuators A Phys.*, vol. 120, no. 2, pp. 370–382, 2005.

[39] C. M. Oddo *et al.*, "Intraneural stimulation elicits discrimination of textural features by artificial fingertip in intact and amputee humans," *Elife*, vol. 5, pp. 1–27, 2016.

[40] P. Valdastri *et al.*, "Integration of a Miniaturised Triaxial Force Sensor in a," *Technology*, vol. 53, no. 11, pp. 2397–2400, 2006.

[41] G. Ciuti, P. Valdastri, A. Menciassi, and P. Dario, "Robotic magnetic steering and locomotion of capsule endoscope for diagnostic and surgical endoluminal procedures," *Robotica*, vol. 28, no. 2, pp. 199–207, 2010.

[42] L. Demling and M. Classen, "Atlas of enteroscopy: endoscopy of the small and large bowel; retrograde cholangio-pancreatography.," *Springer Sci. Bus. Media.*, 2012.

[43] L. J. Sliker, G. Ciuti, M. E. Rentschler, and A. Menciassi, "Frictional resistance model for tissue-capsule endoscope sliding contact in the gastrointestinal tract," *Tribol. Int.*, vol. 102, no. June, pp. 472–484, 2016.

[44] M. Simi, G. Ciuti, S. Tognarelli, P. Valdastri, A. Menciassi, and P. Dario, "Magnetic link design for a robotic laparoscopic camera," *J. Appl. Phys.*, vol. 107, no. 9, p. 09B302, 2010.

[45] C. M. Oddo, L. Beccai, G. G. Muscolo, and M. C.

Carrozza, "A biomimetic MEMS-based tactile sensor array with fingerprints integrated in a robotic fingertip for artificial roughness encoding," *IEEE Int. Conf. Robot. Biomimetics*, no. January, pp. 894–900, 2009.

[46] P. Saccomandi *et al.*, "Tactile piezoresistive sensors for robotic application: Design and metrological characterization," in *2017 IEEE International Instrumentation and Measurement Technology Conference (I2MTC)*, 2017, pp. 1–6.

[47] P. Valdastri *et al.*, "Characterization of a novel hybrid silicon three-axial force sensor," *Sensors Actuators A Phys.*, vol. 123, pp. 249–257, 2005.

[48] C. M. Oddo, P. Valdastri, L. Beccai, S. Roccella, M. C. Carrozza, and P. Dario, "Investigation on calibration methods for multi-axis, linear and redundant force sensors," *Meas. Sci. Technol.*, vol. 18, no. 3, pp. 623–631, 2007.

[49] C. M. Oddo, L. Beccai, G. G. Muscolo, and M. C. Carrozza, "A biomimetic MEMS-based tactile sensor array with fingerprints integrated in a robotic fingertip for artificial roughness encoding," *2009 IEEE Int. Conf. Robot. Biomimetics, ROBIO 2009*, no. January, pp. 894–900, 2009.

[50] G. Vásárhelyi, M. Ádám, É. Vázsonyi, I. Bársony, and C. Dücso, "Effects of the elastic cover on tactile sensor arrays," *Sensors Actuators, A Phys.*, vol. 132, no. 1 SPEC. ISS., pp. 245–251, 2006.

[51] G. Vásárhelyi, B. Fodor, and T. Roska, "Tactile sensing-processing: Interface-cover geometry and the inverse-elastic problem," *Sensors Actuators, A Phys.*, vol. 140, no. 1, pp. 8–18, 2007.

[52] I. D. Johnston, "Mechanical characterization of bulk Sylgard 184 for microfluidics and microengineering," *J. Micromechanics Microengineering*, vol. 24, no. 3, p. 35017, 2014.

[53] M. Clerc and J. Kennedy, "The Particle Swarm — Explosion , Stability , and Convergence in a Multidimensional Complex Space," vol. 6, no. 1, pp. 58–73, 2002.

[54] A. W. Mahoney and J. J. Abbott, "Five-degree-of-freedom manipulation of an untethered magnetic device in fluid using a single permanent magnet with application in stomach capsule endoscopy," *Int. J. Rob. Res.*, vol. 35, no. 1–3, pp. 129–147, 2016.

[55] F. Bianchi *et al.*, "Localization strategies for robotic endoscopic capsules: a review," *Expert Rev. Med. Devices*, vol. 16, no. 5, pp. 381–403, May 2019.

[56] A. Bicchi, G. Canepa, D. De Rossi, P. Iacconi, and E. P. Scillingo, "A sensor-based minimally invasive surgery tool for detecting tissutal elastic properties," *Proc. IEEE Int. Conf. Robot. Autom.*, vol. 1, no. April, pp. 884–888, 1996.

[57] B. Winstone, C. Melhuish, S. Dogramadzi, T. Pipe, and M. Callaway, "A novel bio-inspired tactile tumour detection concept for capsule endoscopy," *Lect. Notes Comput. Sci. (including Subser. Lect. Notes Artif. Intell. Lect. Notes Bioinformatics)*, vol. 8608 LNAI, pp. 442–445, 2014.

[58] F. Bianchi *et al.*, "An innovative robotic platform for magnetically-driven painless colonoscopy," *Ann. Transl. Med.*, vol. 5, no. 21, 2017.

[59] C. H. Chuang, T. H. Li, I. C. Chou, and Y. J. Teng, "Piezoelectric tactile sensor for submucosal tumor detection in endoscopy," *Sensors Actuators, A Phys.*, vol. 244, pp. 299–309, 2016.